



HAL
open science

Mare basalt flooding events surrounding Chang'e-4 landing site as revealed by Zhinyu crater ejecta

Sheng Gou, Zongyu Yue, Kaichang Di, Roberto Bugiolacchi, Meng-Hua Zhu,
Patrick C Pinet, Zhanchuan Cai

► **To cite this version:**

Sheng Gou, Zongyu Yue, Kaichang Di, Roberto Bugiolacchi, Meng-Hua Zhu, et al.. Mare basalt flooding events surrounding Chang'e-4 landing site as revealed by Zhinyu crater ejecta. *Icarus*, 2021, 360, pp.114370. 10.1016/j.icarus.2021.114370 . hal-03441633

HAL Id: hal-03441633

<https://hal.science/hal-03441633v1>

Submitted on 22 Nov 2021

HAL is a multi-disciplinary open access archive for the deposit and dissemination of scientific research documents, whether they are published or not. The documents may come from teaching and research institutions in France or abroad, or from public or private research centers.

L'archive ouverte pluridisciplinaire **HAL**, est destinée au dépôt et à la diffusion de documents scientifiques de niveau recherche, publiés ou non, émanant des établissements d'enseignement et de recherche français ou étrangers, des laboratoires publics ou privés.

1 **Mare basalt flooding events surrounding Chang'e-4 landing site as**
2 **revealed by Zhinyu crater ejecta**

3

4 Sheng GOU^{a, b, c}, Zongyu YUE^{b, d}, Kaichang DI^{b, d, *}, Roberto BUGIOLACCHI^{a, c, f},

5 Meng-Hua ZHU^{a, c}, Patrick C. PINET^e, Zhanchuan CAI^{a, c}

6 ^a State Key Laboratory of Lunar and Planetary Sciences, Macau University of Science
7 and Technology, Macau, China

8 ^b State Key Laboratory of Remote Sensing Science, Aerospace Information Research
9 Institute, Chinese Academy of Sciences, Beijing 100101, China

10 ^c CNSA Macau Center for Space Exploration and Science, Macau, China

11 ^d Center for Excellence in Comparative Planetology, Chinese Academy of Sciences,
12 Hefei 230026, China

13 ^e Institut de Recherche en Astrophysique et Planétologie, University of Toulouse,
14 CNRS, UPS, CNES, UT3, Toulouse, France

15 ^f Earth Sciences, University College London, London, UK

16

17

18

19 *Correspondence to Kaichang DI

20 Email: dikc@radi.ac.cn

21 Tel/Fax: 8610-64868229

22 Address: P.O. Box 9718, No. 20A, Datun Road, Chaoyang District, Beijing, 100101,
23 China

24

25 **Abstract**

26 Von Kármán crater's floor was flooded with mare basalts during [the](#) Imbrian period.
27 This site is the target of China's ongoing Chang'e-4 mission that includes the Yutu-2
28 rover and its instrumental payload. The Zhinyu crater, one of the largest craters within
29 a few tens of kilometers from the landing site, is the product of a fresh impact that
30 excavated subsurface, basaltic materials [onto](#) the surface. The compositional
31 characteristics of the continuous ejecta around the crater vary radially with distance,
32 suggesting possible mineral heterogeneity at depth. At least three main mare flooding
33 phases could have occurred within Von Kármán, producing a basalt layer of at least
34 320 m in thickness. However, a broadly consistent olivine composition (Fo#: 55) of
35 the three proposed basalt layers suggests that the sources of the mare basalts would
36 have been similar in composition, perhaps even consisting of a single magma chamber
37 where magma had time to evolve. The Yutu-2 rover that is edging its way westwards,
38 could in principle test this hypothesis, thus further constraining the thermal history of
39 the Von Kármán crater.

40

41

42 **Keywords:** Zhinyu crater; Von Kármán crater; Mare flooding; Homogenous
43 composition; Single magma chamber;

44 **Highlights**

45

46 1. Three mare flooding events [occurring](#) inside Von Kármán crater during [the](#)
47 Imbrian period are suggested.

48

49 2. The sources of mare basalts are almost homogenous in composition, [perhaps](#)
50 even from a single magma chamber with a moderate [evolution](#).

51

52 3. A refined stratigraphy for low-Ti mare basalts is established and is expected to
53 be verified by the Yutu-2 rover in the near future.

54

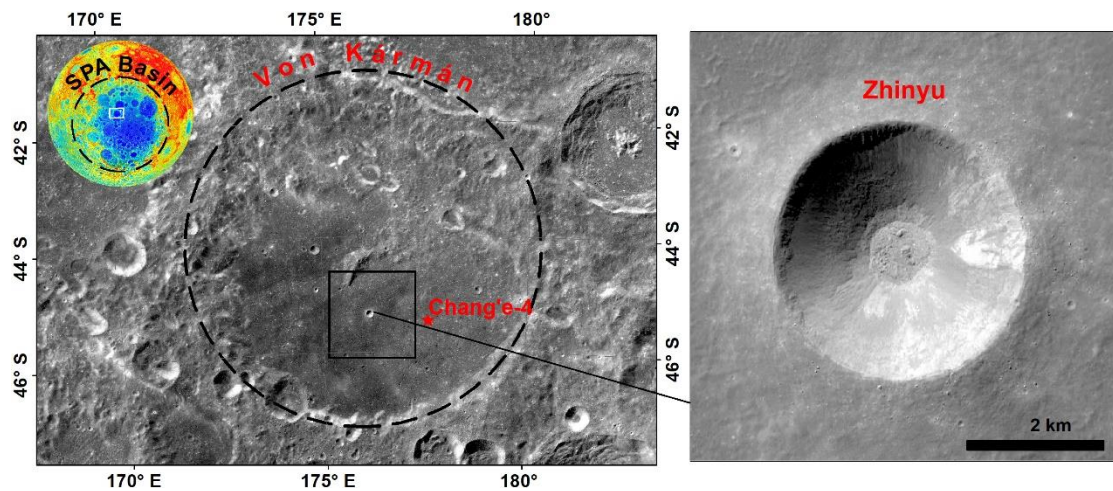
55

56 1. Introduction

57 The Von Kármán crater (~186 km in diameter), lying in the northwest of South
58 Pole-Aitken (SPA) basin on the lunar farside, was formed 3.97 Ga ago in the pre-
59 Nectarian period (Stuart-Alexander, 1978; Yingst et al., 2017). During the Imbrian
60 period, the floor of Von Kármán crater was flooded with several basaltic lava flows
61 (or mare basalts) (Huang et al., 2018; Pasckert et al., 2018; Ling et al., 2019). China's
62 Chang'e-4 probe touched down successfully in the Von Kármán crater at 177.588°E,
63 45.457°S on January 3, 2019, and released the Yutu-2 rover to conduct in situ
64 measurements on this previously unexplored region (Di et al., 2019a; Pinet, 2019).
65 The surface of the Chang'e-4 landing site is generally thought to be mantled by ejecta
66 from the Finsen crater (e.g., Gou et al., 2019; Hu et al., 2019; Gou et al., 2020; Huang
67 et al., 2020; Lin et al., 2020), though the estimation of ejecta thickness from Finsen
68 crater at the landing site is **debated** (Huang et al., 2018; Di et al., 2019b; Fu et al.,
69 2020).

70 Zhinyu (176.15 °E, 45.34 °S), a fresh, simple crater with a diameter of ~3.8 km
71 and a depth of ~ 800 m (Fig. 1) is one of the largest impacts near the Chang'e-4 landing
72 site, lying about 30 km away to the west. The Zhinyu impact penetrated the mare
73 basalts within the Von Kármán crater, thus it opens an exploratory window into the
74 composition and stratigraphy of the subsurface. Hypervelocity impacts exhume
75 materials from the subsurface and deposit them both within and outside the newly
76 formed crater, allowing for investigation. For instance, Fu et al. (2020) targeted 40
77 dark-haloed craters and 77 bright ray craters around the Chang'e-4 landing area and

78 constructed a possible stratigraphy (including a low-Ti mare basalt layer) based on the
79 excavation depths of these craters and their distances from the Finsen crater. Further,
80 observed differences in the ejecta layers would represent geological variations with
81 depth at the target point. For example, Ding et al. (2020) proposed that several fresh
82 craters surrounded by blocky fragments encountered by the Yutu-2 rover might be
83 secondaries of the Zhinyu crater. Since the primary source for the regolith at the
84 Chang'e-4 landing site is reckoned to represent Finsen crater ejecta (compositionally
85 different from mare basalt), caution must be applied in interpreting the in situ
86 measured spectra around these secondary craters. Therefore, the Zhinyu crater ejecta
87 provides a rare opportunity to explore the sub-regolith mare basalts, and should also
88 contribute to the correct interpretation of the in situ measured data by the Yutu-2 rover.



89
90 Fig. 1. Location of the Zhinyu crater inside the Von Kármán crater. The base map
91 is a digital orthophoto map mosaic (7 m/pixel) generated from Chang'e-2 images (Ren
92 et al., 2014). Different colors in the inset represent different heights, with red being the
93 highest and blue being the lowest. The white box shows the boundaries of Fig. 1. The
94 black box frames the area of Fig. 2, Fig. 4, and Fig. 5.

95

96 **2. Data**

97 **2.1 Moon mineralogy mapper spectra**

98 The [Moon Mineralogy Mapper](#) (M³), [which](#) flew onboard India's Chandrayaan-1
99 lunar orbiter, was a push-broom imaging spectrometer operating from the visible into
100 the near-infrared (0.42 - 3.0 μm). M³ observed the lunar surface both in a high-
101 resolution target mode (80 m/pixel; 260 spectral channels) and in a low-resolution
102 global mode (140 m/pixel; 85 spectral channels) from a 100 km orbit (Pieters et al.,
103 2009). The M³ Level 2 spectral reflectance images (REFIMG), which have been
104 photometrically calibrated and thermal emission corrected (Clark et al., 2011; Besse
105 et al., 2013), are used in this study to extract spectra from regions of interest (ROIs)
106 for further detailed analysis (Supplementary Fig. 1).

107 **2.2 Multiband imager products and images**

108 The multiband imager (MI) was a high-resolution imaging camera onboard the
109 Japanese Kaguya lunar orbiter that included separate visible and near infrared sensors
110 (Ohtake et al., 2008). It acquired push-broom images in five bands for [the](#) visible and
111 four bands for the near-infrared spectral ranges (Ohtake et al., 2008). The spatial
112 resolution of the MI [images](#) is 20 m/pixel for the visible bands and 62 m/pixel for the
113 near- infrared bands taken at a nominal orbit altitude of 100 km (Ohtake et al., 2008).
114 The mineral abundance products derived from topographically-corrected MI
115 reflectance data (Lemelin et al., 2016) are used in this study to evaluate compositional
116 variabilities of the mare basalts. As concentrations of TiO₂ and FeO are useful in
117 classifying major lunar rock types (Lucey et al., 1998), derived abundances around the

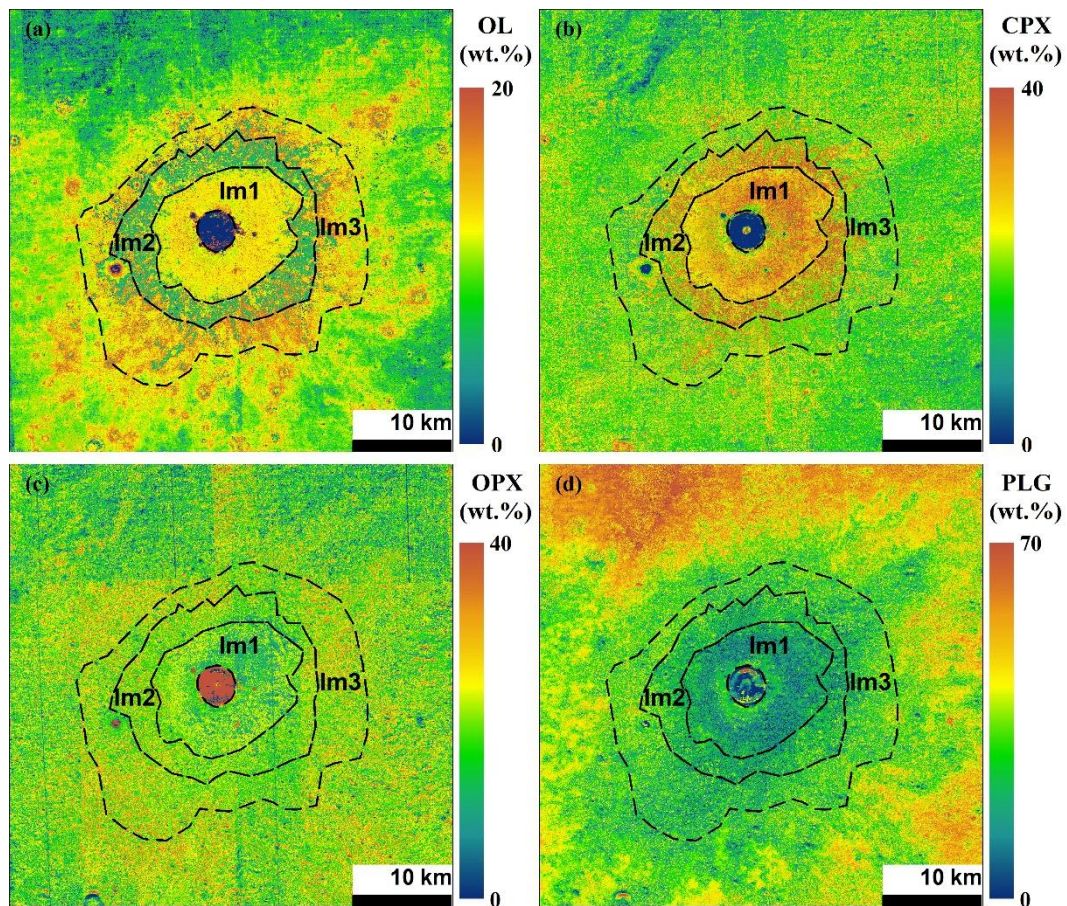
118 Zhinyu crater were produced using the algorithm of Otake et al. (2012) to investigate
119 possible differences.

120

121 **3. Methods**

122 **3.1 Basalt layer identification**

123 There is evidence that the lava infill of the Von Kármán crater occurred during the
124 Imbrian (Im) period (Huang et al., 2018). Inferred TiO_2 content is commonly used as
125 a classifier for basalts: very low Ti (<1.5 wt% TiO_2), low-Ti (1.5–6 wt% TiO_2), and
126 high-Ti (>6 wt% TiO_2) (Hiesinger and Jaumann, 2014). The overall TiO_2 content of
127 the continuous ejecta of Zhinyu crater is relatively low (see section 4.1), making it not
128 suitable for subdivision. Consequently, to evaluate the mineral composition of the
129 ejecta around Zhinyu crater, mineral maps (Fig. 2) of clinopyroxene (CPX),
130 orthopyroxene (OPX), olivine (OL) and plagioclase (PLG) were extracted from the
131 MI derived global map products (Lemelin et al., 2016). It emerges that three rings with
132 varied mineral abundance, in particular for the OL (Fig. 2a), are distributed
133 concentrically around the Zhinyu crater. The boundaries of these three rings are
134 broadly outlined by the OL variation (Lai et al., 2020) and defined in this study as Im1,
135 Im2 and Im3, in the order from the rim outward (Fig. 2). Previous studies have
136 proposed buried mare basalts fields inside the Von Kármán crater (Pasckert et al., 2018;
137 Ling et al., 2019). Here the spectral/mineralogical variations suggest there might have
138 been at least three distinct mare flooding events with a degree of compositional
139 differences.



140

141 Fig. 2. Three mineral abundance variation rings distributed concentrically around
 142 the Zhinyu crater. (a) OL; (b) CPX; (c) OPX; (d) PLG. These MI derived products are
 143 from Lemelin et al. (2016). Upper range boundaries differ to highlight variations.

144

145 3.2 Olivine composition analysis

146 The olivine fraction content of igneous rocks is highly diagnostic for interpreting
 147 the magma source and the degree of petrologic evolution (Isaacson et al., 2011). Based
 148 on the established relation between laboratory spectral absorption features and OL
 149 composition (Sunshine and Pieters, 1998; Isaacson and Pieters, 2010), the relative
 150 Mg/(Mg + Fe) ratio, as known as the forsterite number (Fo#), can be estimated from
 151 the remotely-sensed spectra. Therefore, the average spectrum of each layer was
 152 extracted from M³ images (Supplementary Fig. 1) and deconvolved by the Modified

153 Gaussian Model (MGM) (Supplementary Figs. 2-4) (Sunshine and Pieters, 1993) with
154 different mineral combination configurations (Supplementary Table 1) to estimate
155 mineral modes (Clénet et al., 2011; Clénet et al., 2013). The OL composition is
156 determined by fitting the MGM-derived OL-related absorption centers to a laboratory-
157 derived compositional trend line (Sunshine and Pieters, 1998; Isaacson and Pieters,
158 2010). The uncertainty of the predicted Fo# values that arises from model initial
159 conditions and other error sources, e.g., the low signal-to-noise ratio and low resolution
160 of M^3 spectrum, is estimated to be about 10% Fo# # and possibly more in the case of
161 ternary mineral mixtures (Isaacson and Pieters, 2010; Pinet et al., 2018; Pinet et al.,
162 2019).

163

164 **3.3 Basalt layer thickness estimation**

165 For a lunar simple crater with a diameter smaller than 15 km, the maximum
166 excavation depth (H_{exc}) is approximately 1/10 of the transient crater diameter (D_t),
167 which is about 0.84 times the rim-to-rim diameter (D), i.e., $D_t = 0.84D$ (Melosh, 1989).
168 The ejecta apron of an impact crater is composed of target materials excavated during
169 the excavation stage (Melosh, 1989). They are deposited around the crater following an
170 inverted pre-impact stratigraphy of the underlying bedrock: the materials from the
171 shallower depths tend to be thrown farther away from the crater rim than materials
172 excavated from deeper layers (Thomson et al., 2009). The ejecta becomes thinner and
173 more mixed with local mature regolith with increasing radial distance (Melosh, 1989).
174 The average radius of continuous ejecta blanket (R_{ce}) can be estimated from crater

175 radius (R) using the relation $R_{ce} = (2.348_{-0.454}^{+0.564})R^{1.006}$ (Moore et al., 1974).

176 Although many laboratory experiments and numerical simulations have studied
177 impacts into layered targets (e.g., Stöffler et al., 1975; Senft and Stewart, 2007; Prieur
178 et al., 2018), little work has been done to specifically address the relationship between
179 the radial position of ejecta on the upper surface of the continuous ejecta blanket and
180 depth of excavation in layered targets (e.g., Baratoux et al., 2007; Thomson et al., 2009).
181 As a first approximation in this study, it's assumed that continuous ejecta at the farthest
182 distance (D_{max}) comes from the surface, and the radial position of the continuous ejecta
183 blanket is inversely related to the excavation depth, i.e., $(H_{exc} - S_{ce})/H_{exc} = D/D_{max}$.
184 Therefore, the source depth of continuous ejecta blanket (S_{ce}) at a given radial position
185 (D) is estimated by equation $S_{ce} = H_{exc} - (D * H_{exc} / D_{max})$.

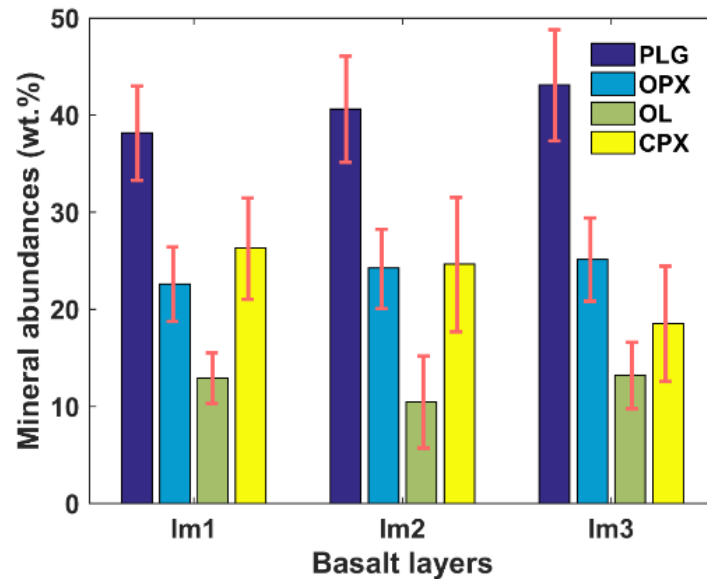
186

187 **4. Results and discussions**

188 **4.1 Composition variations**

189 Results of the MI-derived mineral abundances (Lemelin et al., 2016) for the three
190 layers (in the order Im1, Im2, and Im3) show that the PLG abundance increases from
191 38.2% to 43.1%, the CPX decreases from 26.3% to 18.8%, the OPX increases from
192 22.6% to 25.2%, and the OL decreases from 12.9% to 10.5% and then increases to
193 13.2%. The mineral abundances almost fall within each other's standard deviation (Fig.
194 3), suggesting variations to be marginal. For example, the average CPX abundances for
195 Im1, Im2 and Im3 are $\sim 26.3 \pm 5.3\%$, $\sim 24.8 \pm 6.9\%$ and $\sim 18.8 \pm 6.2\%$, respectively. Also,
196 the average OL abundances are $\sim 12.9 \pm 2.6\%$, $\sim 10.5 \pm 4.7\%$ and $\sim 13.2 \pm 3.4\%$,
197 respectively. MGM fitting results reveal that Fo# values derived from OL-related

198 absorptions are ~ 55 , suggesting that the OL to be relatively homogenous within the
199 sampled units.



200

201 Fig. 3. Mineral abundances of the identified three basalt layers. The error bars

202 show the standard deviation of each mineral abundance.

203

204 The average FeO contents for Im1, Im2 and Im3 are $\sim 17.1 \pm 0.4\%$, $\sim 16.6 \pm 0.4\%$ and

205 $\sim 15.9 \pm 0.5\%$, respectively. Also, the average TiO₂ contents are $\sim 1.5 \pm 0.4\%$, $\sim 1.7 \pm 0.3\%$

206 and $\sim 1.6 \pm 0.3\%$, respectively (Fig. 4). Compared with lunar basalts sampled by Apollo

207 and Luna missions or in situ measured by a rover (for example, the FeO and TiO₂

208 contents of basalt measured by the Chang'e-3 rover are ~ 22.8 wt% and ~ 5.0 wt%,

209 respectively (Ling et al., 2015)), the identified three layers generally have relatively

210 low FeO and TiO₂ contents.

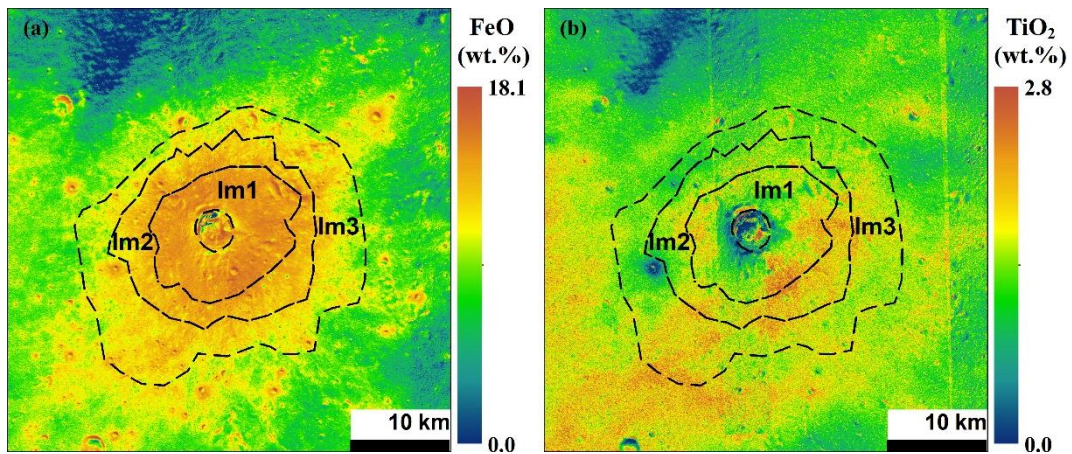
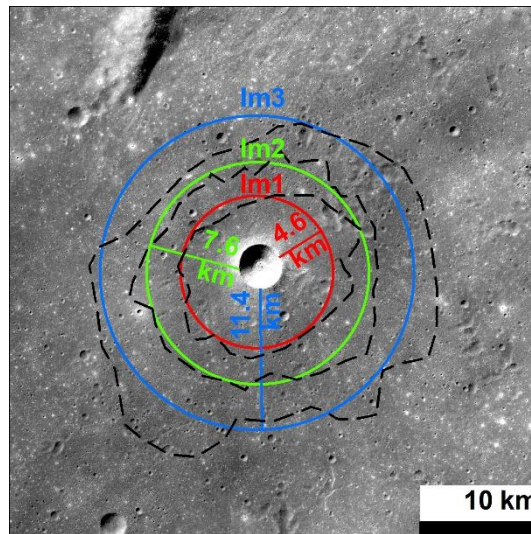


Fig. 4. FeO and TiO₂ contents of identified three mare basalt layers.

4.2 The thickness of the basalt layers

Based on the excavation depth of impact crater (section 3.3), the maximum excavation depth (H_{exc}) and radius of continuous ejecta blanket (R_{ce}) of Zhinyu crater are about 320 m and 11.4 km, respectively. Because the extents of the identified three layers are outlined by irregular polygonal rings, the average ejecta range from each layer is approximated by the difference between the radius of a fitted circle of each layer and the radius of Zhinyu crater (Fig. 5). The results show that the extents of all the three identified layers are roughly within the maximum extent of the continuous ejecta. The average ejecta ranges of Im1, Im2 and Im3 are about 4.6 km, 7.6 km and 11.4 km, indicating the extent of each layer is about 3.4, 5 and 7 times of Zhinyu crater's radius, respectively. Therefore, the thicknesses of the proposed three basalt layers (from top to bottom) are estimated to be about 107 m, 84 m and 129 m, respectively. It is important to note that it cannot be determined whether the Zhinyu impact had penetrated the entire Im1 layer in this study. Therefore, the overall thickness of three mare basalt layers is estimated to be at least 320 m. Because large portions of the northeastern region of the Von Kármán crater floor are mantled by the ejecta from the

229 Finsen crater, and the area of the mare unit is about 6145 km² (Pasckert et al., 2018), a
230 minimum mare volume is thus estimated to be about 1966 km³.



231

232 Fig. 5. Approximation of ejecta range around Zhinyu crater.

233

234 Ling et al. (2019) divided the mare region inside the Von Kármán crater into Low-
235 Ti unit ($1.5 \text{ wt}\% < \text{TiO}_2 < 3 \text{ wt}\%$) and Finsen ejecta unit ($\text{TiO}_2 < 1.5 \text{ wt}\%$). Crater size-
236 frequency distribution (CSFD) measurements of the Low-Ti mare unit show three
237 absolute model ages (AMAs), i.e., 3.38 Ga, 3.57 Ga, and 3.72 Ga (Ling et al., 2019).
238 These AMAs indicate there might be older buried lava flows in the Von Kármán crater
239 (Pasckert et al., 2018; Ling et al., 2019), and the composition variations (Fig. 3)
240 highlighted in this study indicate the recent erupted basalt (Im3) might have a lower
241 CPX/OPX ratio than the older basalts (Im1). The kink (deflection diameter) between
242 the youngest (3.38 Ga) and oldest (3.72) isochron curves is ~1 km, suggesting the
243 thickness of buried lava flows to be >100 m (Ling et al., 2019). The estimated total
244 basalt thickness ($\geq 320 \text{ m}$) in this study agrees with this estimate. As a result, a refined
245 stratigraphic sequence for the low-Ti mare basalts (Ling et al., 2019; Qiao et al., 2019;

246 Fu et al., 2020) is proposed in this study, from top to bottom: Im3 (~107 m), Im2 (~84
247 m), and Im1 (≥ 129 m).

248 A Lunar Penetrating Radar (LPR), with two work frequency channels (channel 1,
249 60 MHz; channel 2, 500 MHz), is part of the instrumentation on the Yutu-2 rover to
250 study the subsurface structure of its traversing area (Fang et al., 2014; Jia et al., 2018).
251 Initial interpretations of the data indicate that there are several subsurface layers/units,
252 pointing to a complex thermal history. For example, the high-frequency LPR data reveal
253 that the shallow subsurface at the landing area is roughly composed of three layers (Lai
254 et al., 2019; Li et al., 2020; Zhang et al., 2020a; Zhang et al., 2020b): a topmost fine-
255 grained regolith layer (depth, 0 to 12 m), an intermediate layer consisting of coarse
256 materials with embedded rocks (12 to 24 m), and a bottom layer composed of
257 alternating coarse and fine materials (24 to 40 m). As of November 22, 2020, the Yutu-
258 2 rover had already operated for 24 lunar days and traversed about 590 m on the Finsen
259 ejecta unit within the Von Kármán crater. The rover is currently about 30 km away from
260 the Zhinyu crater. The collected low-frequency LPR channel has the maximum
261 detection depth of ~330m (Lai et al., 2020), possibly up to ~500 m (Zhang et al., 2020a).
262 However, due to the low thickness resolution (~10 m) of the LPR low-frequency data
263 and different processing procedures, the deep multi-layered stratigraphic structure
264 revealed by the low-frequency LPR data is not entirely consistent between most of the
265 studies, including Lai et al. (2020), Zhang et al. (2020a), and Zhang et al. (2020b).
266 Nevertheless, the basaltic stratigraphic sequence at the Zhinyu crater proposed in this
267 study roughly corresponds to the D and E layers in the work of Lai et al. (2020). The

268 rover will continue to traverse westward and it is planned to reach the mare basalt area
269 in the future. The proposed stratigraphic sequence and basalt thickness are expected to
270 be validated by the LPR data, which will provide ground truth and should contribute to
271 a fuller understanding of the basalt thermal history of the Von Kármán crater.

272

273 **4.3 Implications for magma evolution**

274 The ejecta under investigation is composed of materials exhumed by the Zhinyu
275 crater during formation, a process that inverts the target's stratigraphical sequence.
276 Therefore, the variation of ejecta composition along the radial distances around Zhinyu
277 crater reflects the compositional variation of the basalt source at different stratigraphic
278 depths. A fairly homogenous OL composition (Fo#: 55) of the three layers indicates the
279 sources of these mare basalts (≥ 320 m in thickness) are almost homogenous in
280 composition, or might even be from a single magma chamber. Generally, for primary
281 magmas, forsteritic (high Fo#) OL is indicative of a primitive source, and more fayalitic
282 (low Fo#) OL is indicative of an evolved source (Basaltic Volcanism Study Project,
283 1981). The predicted Fo# value points to a moderate magma evolution. The small
284 mineral abundance differences (Fig. 3) among layers may indicate there were at least
285 three mare flooding events occurred inside Von Kármán crater during the Imbrian
286 period, with two dome-like structures being the possible latest volcanic vents of these
287 basalts (Qiao et al., 2019).

288

289 **5. Conclusion**

290 China's Chang'e-4 probe landed inside the Von Kármán crater, whose floor was

291 flooded with mare basalts during the Imbrian period. Zhinyu, a fresh impact crater, is
292 the largest close to the landing site. The materials exhumed by the blast would have
293 distributed the ejecta around the crater, exposing the stratigraphy sequence of the
294 underlying basaltic rock layer(s). The mineral abundances derived from multispectral
295 data, vary radially and discontinuously from the rim craters outwards, forming
296 compositionally distinguished annuli. In particular, variations in the mineral olivine and
297 clinopyroxene abundances support the idea that there could be at least three distinct
298 basalt layers (named Im1, Im2, and Im3 from bottom to top) within the Von Kármán
299 crater. The thickness of each layer is estimated by an empirical relation according to the
300 processes of impact excavation and ejecta deposition, i.e., the shallow material deposits
301 at the further distance whereas the deep material deposits around the crater. As it cannot
302 be determined in this study whether the Zhinyu impact penetrated through the entire
303 Im1 layer, the total thickness of the three basalt layers is estimated to be at least 320 m.
304 However, the minor differences noted in the mineral abundances and the fairly
305 consistent olivine compositions (Fo#: 55) of these three layers indicate the sources of
306 these mare basalts to be comparable in composition, perhaps even from a single magma
307 chamber where the magma underwent only moderate [evolution](#). The westward
308 traversing Yutu-2 rover may provide ground truth for the findings in this study, which
309 would contribute to the understanding of the thermal history of the Von Kármán crater.

310

311 **Declaration of competing interest**

312 The authors declare that they have no known competing financial interests

313 or personal relationships that could have appeared to influence the work
314 reported in this article.

315

316 **Acknowledgments**

317 The M³ data are from PDS Geoscience Node ([https://pds-
318 geosciences.wustl.edu/](https://pds-geosciences.wustl.edu/)). The MI data are from Selene Data Archive
319 (<http://l2db.selene.darts.isas.jaxa.jp/>). The MI-derived mineral maps are from
320 (<https://astrogeology.usgs.gov/maps/lunar-kaguya-multiband-imager-mosaics>).

321 This work was supported by the Strategic Priority Research Program of Chinese
322 Academy of Sciences (grant No. XDB41000000), National Natural Science
323 Foundation of China (grant Nos. 41702354 and 41941003), Macao Young Scholars
324 Program (grant No. AM201902), and Science and Technology Development Fund of
325 Macau (grant No. 131/2017/A3).

326

327 **Supplementary material**

328 Supplementary material associated with this article can be found in the
329 online version.

330

331 **References**

332 Baratoux, D., Pinet, P., Gendrin, A., Kanner, L., Mustard, J., Daydou, Y., Vaucher,
333 J., Bibring, J.-P., 2007. Mineralogical structure of the subsurface of Syrtis
334 Major from OMEGA observations of lobate ejecta blankets. *Journal of*

335 Geophysical Research: Planets. 112 (E8), E08S05.

336 Besse, S., Yokota, Y., Boardman, J., Green, R., Haruyama, J., Isaacson, P., Mall,
337 U., Matsunaga, T., Ohtake, M., Pieters, C., Staid, M., Sunshine, J.,
338 Yamamoto, S., 2013. One Moon, many measurements 2: Photometric
339 corrections. *Icarus*. 226 (1), 127-139.

340 Basaltic Volcanism Study Project, 1981. *Basaltic Volcanism on the Terrestrial*
341 *Planets*. Pergamon Press, New York.

342 Clénet, H., Pinet, P. C., Daydou, Y., Heuripeau, F., Rosemberg, C., Baratoux, D.,
343 Chevrel, S., 2011. A new systematic approach using the Modified
344 Gaussian Model: Insight for the characterization of chemical composition
345 of olivines, pyroxenes and olivine–pyroxene mixtures. *Icarus*. 213 (1),
346 404-422.

347 Clénet, H., Pinet, P., Ceuleneer, G., Daydou, Y., Heuripeau, F., Rosemberg, C.,
348 Bibring, J. P., Bellucci, G., Altieri, F., Gondet, B., 2013. A systematic
349 mapping procedure based on the Modified Gaussian Model to
350 characterize magmatic units from olivine/pyroxenes mixtures:
351 Application to the Syrtis Major volcanic shield on Mars. *Journal of*
352 *Geophysical Research: Planets*. 118 (8), 1632-1655.

353 Clark, R. N., Pieters, C. M., Green, R. O., Boardman, J. W., Petro, N. E., 2011.
354 Thermal removal from near-infrared imaging spectroscopy data of the
355 Moon. *Journal of Geophysical Research: Planets*. 116 (E6), E00G16.

356 Di, K., Liu, Z., Liu, B., Wan, W., Peng, M., Wang, Y., Gou, S., Yue, Z., Xn, X.,

357 Jia, M., Niu, S., 2019a. Chang'e-4 lander localization based on multi-
358 source data. *Journal of Remote Sensing*. 23 (1), 177-184.

359 Di, K., Zhu, M.-H., Yue, Z., Lin, Y., Wan, W., Zhaoqin Liu, Gou, S., Liu, B.,
360 Man Peng, Wang, Y., Niu, S., Zhang, J., Li, J., Xie, J., Xi, L., Yang, J.,
361 Xue, B., 2019b. Topographic evolution of Von Kármán crater revealed by
362 the lunar rover Yutu-2. *Geophysical Research Letters*. 46 (22), 12764-
363 12770.

364 Ding, C., Xiao, Z., Wu, B., Li, Y., Prieur, N. C., Cai, Y., Su, Y., Cui, J., 2020.
365 Fragments Delivered by Secondary Craters at the Chang'E-4 Landing Site.
366 *Geophysical Research Letters*. 47 (7), e2020GL087361.

367 Fang, G.-Y., Zhou, B., Ji, Y.-C., Zhang, Q.-Y., Shen, S.-X., Li, Y.-X., Guan, H.-
368 F., Tang, C.-J., Gao, Y.-Z., Lu, W., Ye, S.-B., Han, H.-D., Zheng, J., Wang,
369 S.-Z., 2014. Lunar Penetrating Radar onboard the Chang'e-3 mission.
370 *Research in Astronomy and Astrophysics*. 14 (12), 1607-1622.

371 Fu, X.-H., Qiao, L., Zhang, J., Ling, Z.-C., Li, B., 2020. The subsurface structure
372 and stratigraphy of the Chang'E-4 landing site: orbital evidence from
373 small craters on the Von Kármán crater floor. *Research in Astronomy and*
374 *Astrophysics*. 20 (1), 8(12pp).

375 Gou, S., Di, K., Yue, Z., Liu, Z., He, Z., Xu, R., Lin, H., Liu, B., Peng, M., Wan,
376 W., Wang, Y., Liu, J., 2019. Lunar deep materials observed by Chang'e-4
377 rover. *Earth and Planetary Science Letters*. 528, 115829.

378 Gou, S., Di, K., Yue, Z., Liu, Z., He, Z., Xu, R., Liu, B., Peng, M., Wan, W.,

379 Wang, Y., Liu, J., 2020. Forsteritic olivine and magnesium-rich
380 orthopyroxene materials measured by Chang'e-4 rover. *Icarus*. 345,
381 113776.

382 Hiesinger, H., Jaumann, R., 2014 Chapter 23 - The Moon. In: Spohn, T., Breuer,
383 D., Johnson, T. V., (Eds.), *Encyclopedia of the Solar System* (Third
384 Edition). Elsevier, Boston, pp. 493-538.

385 Hu, X., Ma, P., Yang, Y., Zhu, M.-H., Jiang, T., Lucey, P. G., Sun, L., Zhang, H.,
386 Li, C., Xu, R., He, Z., Lin, H., Huang, C., Sun, Y., 2019. Mineral
387 abundances inferred from in-situ reflectance measurements of Chang'E-
388 4 landing site in South Pole-Aitken basin. *Geophysical Research Letters*.
389 46, 9439–9447.

390 Huang, J., Xiao, Z., Flahaut, J., Martinot, M., Head, J., Xiao, X., Xie, M., Xiao,
391 L., 2018. Geological Characteristics of Von Kármán Crater, Northwestern
392 South Pole-Aitken Basin: Chang'E-4 Landing Site Region. *Journal of*
393 *Geophysical Research: Planets*. 123 (7), 1684-1700.

394 Huang, J., Xiao, Z., Xiao, L., Horgan, B., Hu, X., Lucey, P., Xiao, X., Zhao, S.,
395 Qian, Y., Zhang, H., Li, C., Xu, R., He, Z., Yang, J., Xue, B., He, Q.,
396 Zhong, J., Lin, H., Huang, C., Xie, J., 2020. Diverse rock types detected
397 in the lunar South Pole–Aitken Basin by the Chang'E-4 lunar mission.
398 *Geology*. 48, 723–727.

399 Isaacson, P. J., Pieters, C. M., 2010. Deconvolution of lunar olivine reflectance
400 spectra: Implications for remote compositional assessment. *Icarus*. 210

401 (1), 8-13.

402 Isaacson, P. J., Pieters, C. M., Besse, S., Clark, R. N., Head, J. W., Klima, R. L.,
403 Mustard, J. F., Petro, N. E., Staid, M. I., Sunshine, J. M., 2011. Remote
404 compositional analysis of lunar olivine- rich lithologies with Moon
405 Mineralogy Mapper (M³) spectra. *Journal of Geophysical Research: Planets*. 116 (E6), E00G11.

407 Jia, Y., Zou, Y., Ping, J., Xue, C., Yan, J., Ning, Y., 2018. The scientific objectives
408 and payloads of Chang'E-4 mission. *Planetary and Space Science*. 162,
409 207-215.

410 Lai, J., Xu, Y., Zhang, X., Xiao, L., Yan, Q., Meng, X., Zhou, B., Dong, Z., Zhao,
411 D., 2019. Comparison of Dielectric Properties and Structure of Lunar
412 Regolith at Chang'e-3 and Chang'e-4 Landing Sites Revealed by Ground
413 Penetrating Radar. *Geophysical Research Letters*. 46, 12783-12793.

414 Lai, J., Xu, Y., Bugiolacchi, R., Meng, X., Xiao, L., Xie, M., Liu, B., Di, K.,
415 Zhang, X., Zhou, B., Shen, S., Xu, L., 2020. First look by the Yutu-2 rover
416 at the deep subsurface structure at the lunar farside. *Nature
417 Communications*. 11 (1), 3426.

418 Lemelin, M., Lucey, P. G., Gaddis, L. R., Hare, T., Ohtake, M., 2016. Global map
419 products from the Kaguya Multiband Imager at 512 ppd: Minerals, FeO
420 and OMAT. 47th Lunar and Planetary Science Conference, the
421 Woodlands, Texas, pp. 2994.

422 Li, C., Su, Y., Pettinelli, E., Xing, S., Ding, C., Liu, J., Ren, X., Lauro, S. E.,

423 Soldovieri, F., Zeng, X., Gao, X., Chen, W., Dai, S., Liu, D., Zhang, G.,
424 Zuo, W., Wen, W., Zhang, Z., Zhang, X., Zhang, H., 2020. The Moon's
425 farside shallow subsurface structure unveiled by Chang'E-4 Lunar
426 Penetrating Radar. *Science Advances*. 6 (9), eaay6898.

427 Lin, H., He, Z., Yang, W., Lin, Y., Xu, R., Zhang, C., Zhu, M.-H., Chang, R.,
428 Zhang, J., Li, C., Lin, H., Liu, Y., Gou, S., Wei, Y., Hu, S., Xue, C., Yang,
429 J., Zhong, J., Fu, X., Wan, W., Zou, Y., 2020. Olivine-norite rock detected
430 by the lunar rover Yutu-2 likely crystallized from the SPA impact melt
431 pool. *National Science Review*. 7, 913–920.

432 Ling, Z., Jolliff, B. L., Wang, A., Li, C., Liu, J., Zhang, J., Li, B., Sun, L., Chen,
433 J., Xiao, L., Liu, J., Ren, X., Peng, W., Wang, H., Cui, X., He, Z., Wang,
434 J., 2015. Correlated compositional and mineralogical investigations at the
435 Chang'e-3 landing site. *Nature Communications*. 6, 8880.

436 Ling, Z., Qiao, L., Liu, C., Cao, H., Bi, X., Lu, X., Zhang, J., Fu, X., Li, B., Liu,
437 J., 2019. Composition, mineralogy and chronology of mare basalts and
438 non-mare materials in Von Kármán crater: Landing site of the Chang'E-4
439 mission. *Planetary and Space Science*. 179, 104741.

440 Lucey, P. G., Taylor, G. J., Hawke, B. R., Spudis, P. D., 1998. FeO and TiO₂
441 concentrations in the South Pole-Aitken basin: Implications for mantle
442 composition and basin formation. *Journal of Geophysical Research:*
443 *Planets*. 103 (E2), 3701-3708.

444 Melosh, H. J., 1989. *Impact Cratering: A geologic process*. Oxford University

445 Press, New York.

446 Moore, H. J., Hodges, C. A., Scott, D. H., 1974. Multiringed basins - illustrated
447 by Orientale and associated features. 5th Lunar Science Conference,
448 Houston, Texas, pp. 71-100.

449 Ohtake, M., Haruyama, J., Matsunaga, T., Kodama, S., Morota, T., Yokota, Y.,
450 2008. Scientific objectives and specification of the SELENE Multiband
451 Imager. *Advances in Space Research*. 42 (2), 301-304.

452 Otake, H., Ohtake, M., Hirata, N., 2012. Lunar Iron and Titanium Abundance
453 Algorithms Based on SELENE (Kaguya) Multiband Imager Data. 43rd
454 Lunar and Planetary Science Conference, the Woodlands, Texas, pp. 1905.

455 Pasckert, J. H., Hiesinger, H., van der Bogert, C. H., 2018. Lunar farside
456 volcanism in and around the South Pole–Aitken basin. *Icarus*. 299, 538-
457 562.

458 Pieters, C. M., Boardman, J., Buratti, B., Chatterjee, A., Clark, R., Glavich, T.,
459 Green, R., Head, J., Isaacson, P., Malaret, E., 2009. The Moon mineralogy
460 mapper (M3) on Chandrayaan-1. *Current Science*. 96 (4), 500-505.

461 Pinet, P. C., Chevrel, S. D., Daydou, Y. H., 2018. Characterization of the
462 Olivine/Plagioclase Mineralogy at Copernicus Crater from MGM
463 Deconvolution of M3 Observations. 49th Lunar and Planetary Science
464 Conference, the Woodlands, Texas, pp. 1899.

465 Pinet, P. C., 2019. The Moon's mantle unveiled. *Nature*. 569 (7756), 338-339.

466 Pinet, P. C., Chevrel, S. D., Daydou, Y. H., 2019. Reassessing the relationship

467 between olivine composition and reflectance Spectroscopy from
468 advanced MGM deconvolution. 50th Lunar and Planetary Science
469 Conference, the Woodlands, Texas, pp. 1806.

470 Prieur, N. C., Rolf, T., Wünnemann, K., Werner, S. C., 2018. Formation of
471 Simple Impact Craters in Layered Targets: Implications for Lunar Crater
472 Morphology and Regolith Thickness. *Journal of Geophysical Research:*
473 *Planets*. 123 (6), 1555-1578.

474 Qiao, L., Ling, Z., Fu, X., Li, B., 2019. Geological characterization of the
475 Chang'e-4 landing area on the lunar farside. *Icarus*. 333, 37-51.

476 Ren, X., Liu, J. J., Wang, F. F., Wang, W. R., Mu, L. L., Li, H. H., 2014. A New
477 lunar global topographic map products from Chang'E-2 Stereo Camera
478 Image Data. European Planetary Science Congress, Cascais, Portugal, pp.
479 EPSC2014-344.

480 Senft, L. E., Stewart, S. T., 2007. Modeling impact cratering in layered surfaces.
481 *Journal of Geophysical Research: Planets*. 112 (E11), E11002.

482 Stöffler, D., Gault, D. E., Wedekind, J., Polkowski, G., 1975. Experimental
483 hypervelocity impact into quartz sand: Distribution and shock
484 metamorphism of ejecta. *Journal of Geophysical Research*. 80 (29), 4062-
485 4077.

486 Stuart-Alexander, D. E., 1978. Geologic map of the central far side of the Moon.

487 Sunshine, J. M., Pieters, C. M., 1993. Estimating modal abundances from the
488 spectra of natural and laboratory pyroxene mixtures using the modified

489 Gaussian model. *Journal of Geophysical Research*. 98 (E5), 9075-9087.

490 Sunshine, J. M., Pieters, C. M., 1998. Determining the composition of olivine
491 from reflectance spectroscopy. *Journal of Geophysical Research*. 103
492 (E6), 13675-13688.

493 Thomson, B. J., Grosfils, E. B., Bussey, D. B. J., Spudis, P. D., 2009. A new
494 technique for estimating the thickness of mare basalts in Imbrium Basin.
495 *Geophysical Research Letters*. 36 (12), L12201.

496 Yingst, R. A., Chuang, F. C., Berman, D. C., Mest, S. C., 2017. Geologic
497 Mapping of the Planck Quadrangle of the Moon (LQ-29). 48th Lunar and
498 Planetary Science Conference, the Woodlands, Texas, pp. 1680.

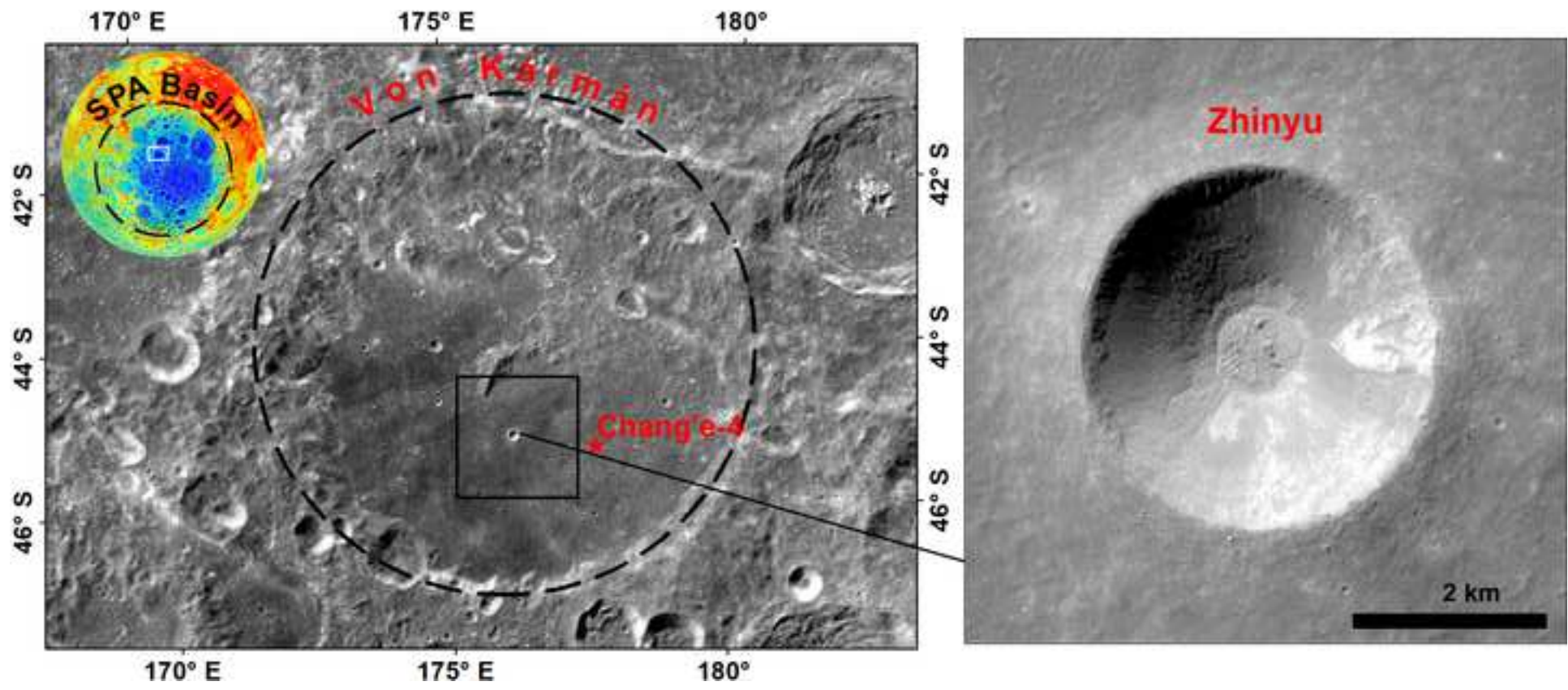
499 Zhang, J., Zhou, B., Lin, Y., Zhu, M.-H., Song, H., Dong, Z., Gao, Y., Di, K.,
500 Yang, W., Lin, H., Yang, J., Liu, E., Wang, L., Lin, Y., Li, C., Yue, Z., Yao,
501 Z., Ouyang, Z., 2020a. Lunar regolith and substructure at Chang'E-4
502 landing site in South Pole–Aitken basin. *Nature Astronomy*.
503 <https://doi.org/10.1038/s41550-020-1197-x>.

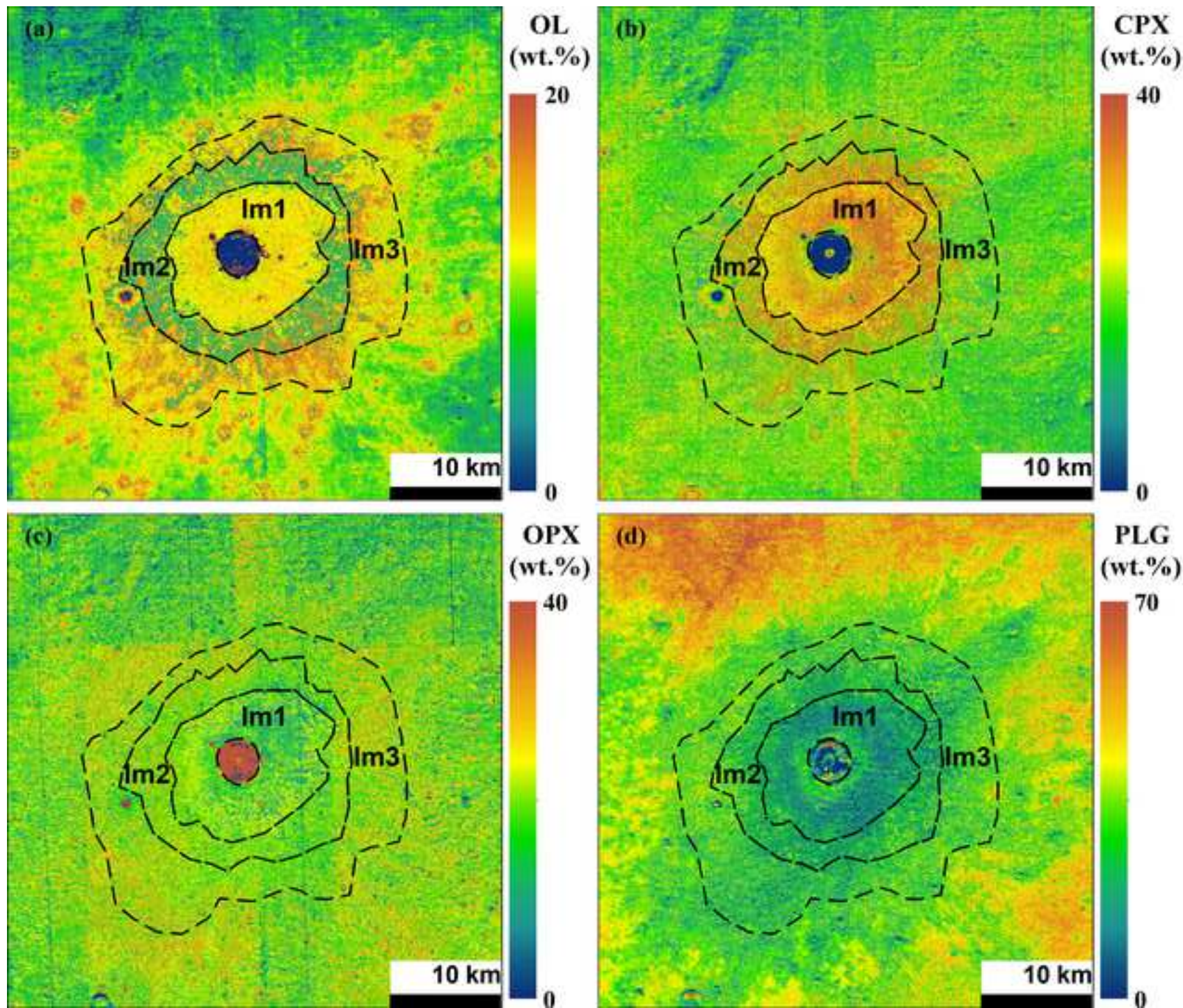
504 Zhang, L., Li, J., Zeng, Z., Xu, Y., Liu, C., Chen, S., 2020b. Stratigraphy of the
505 Von Kármán Crater Based on Chang'E-4 Lunar Penetrating Radar Data.
506 *Geophysical Research Letters*. 47 (15), e2020GL088680.

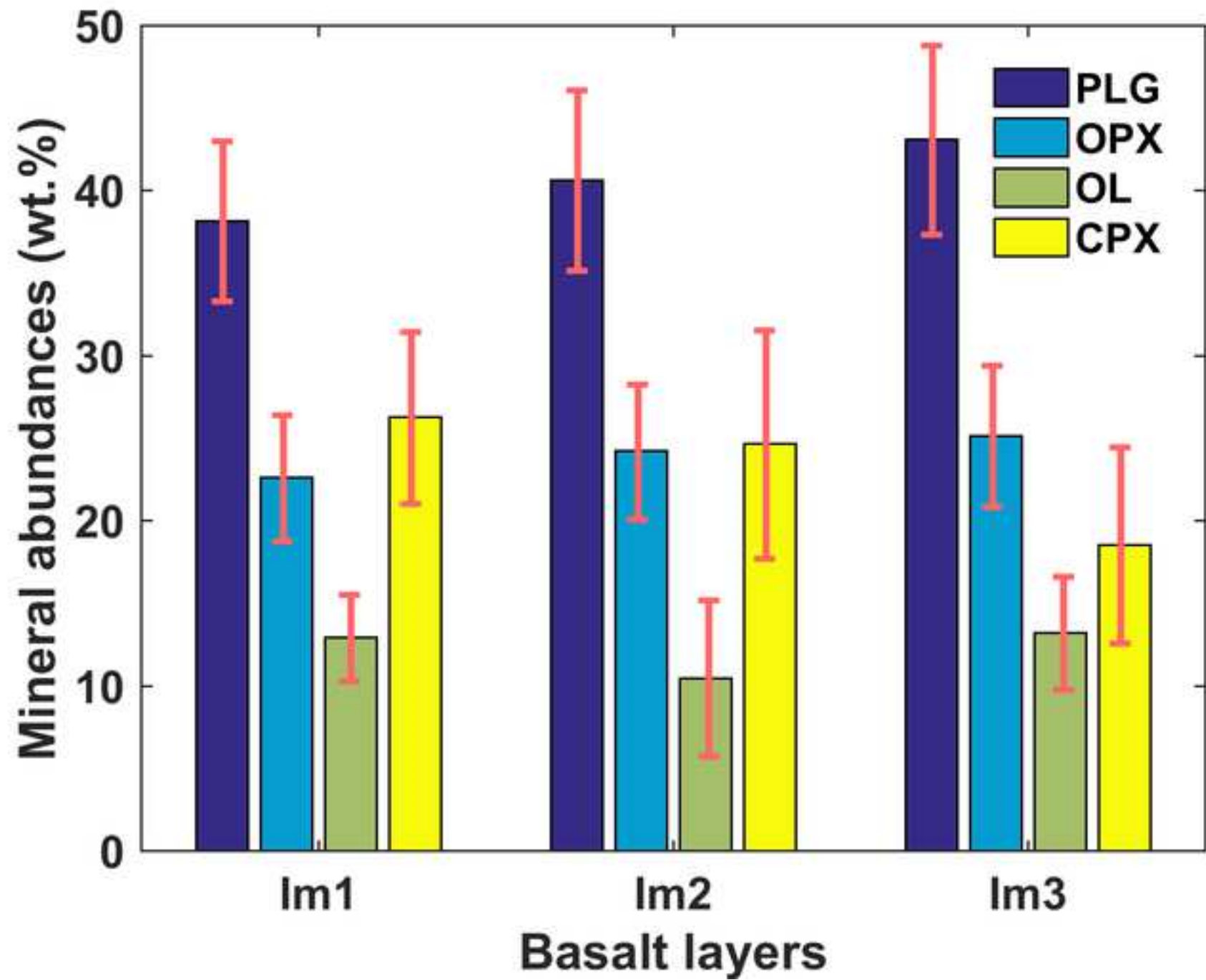
507

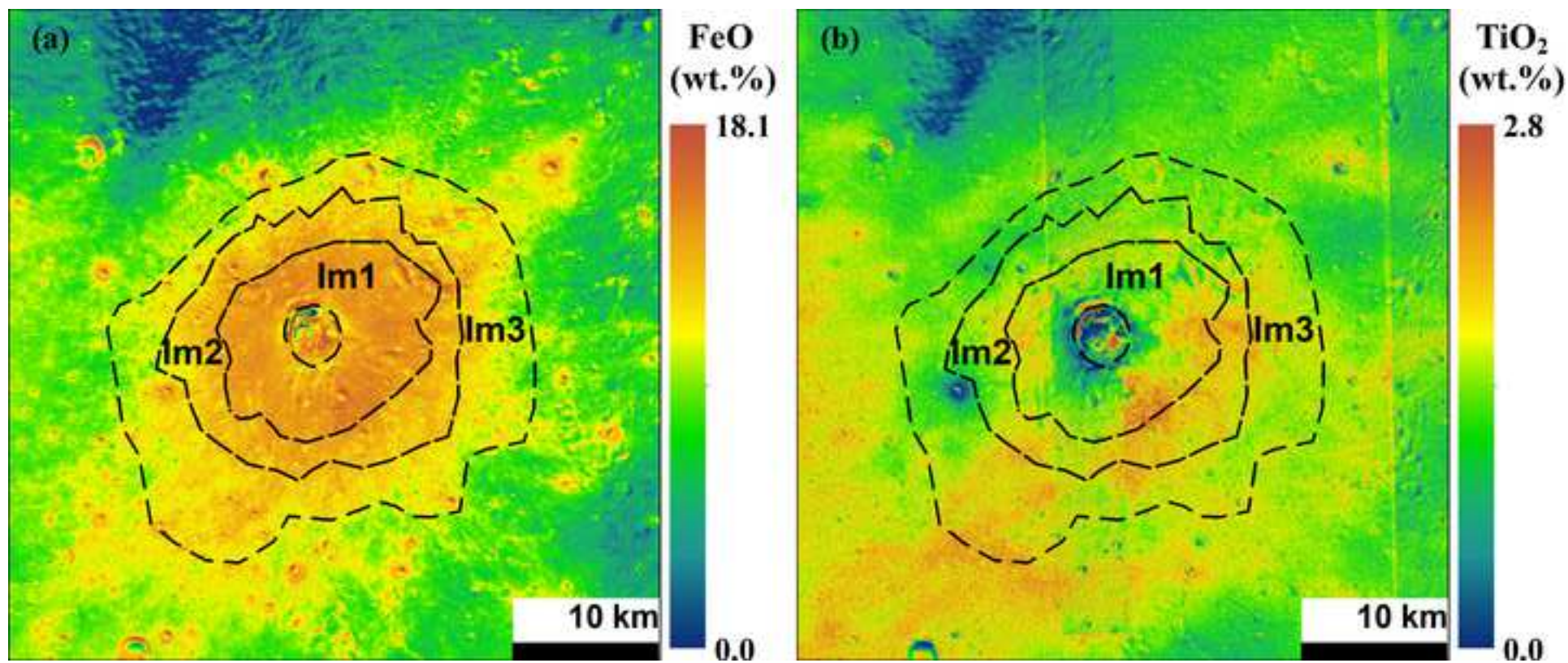
Figure 1

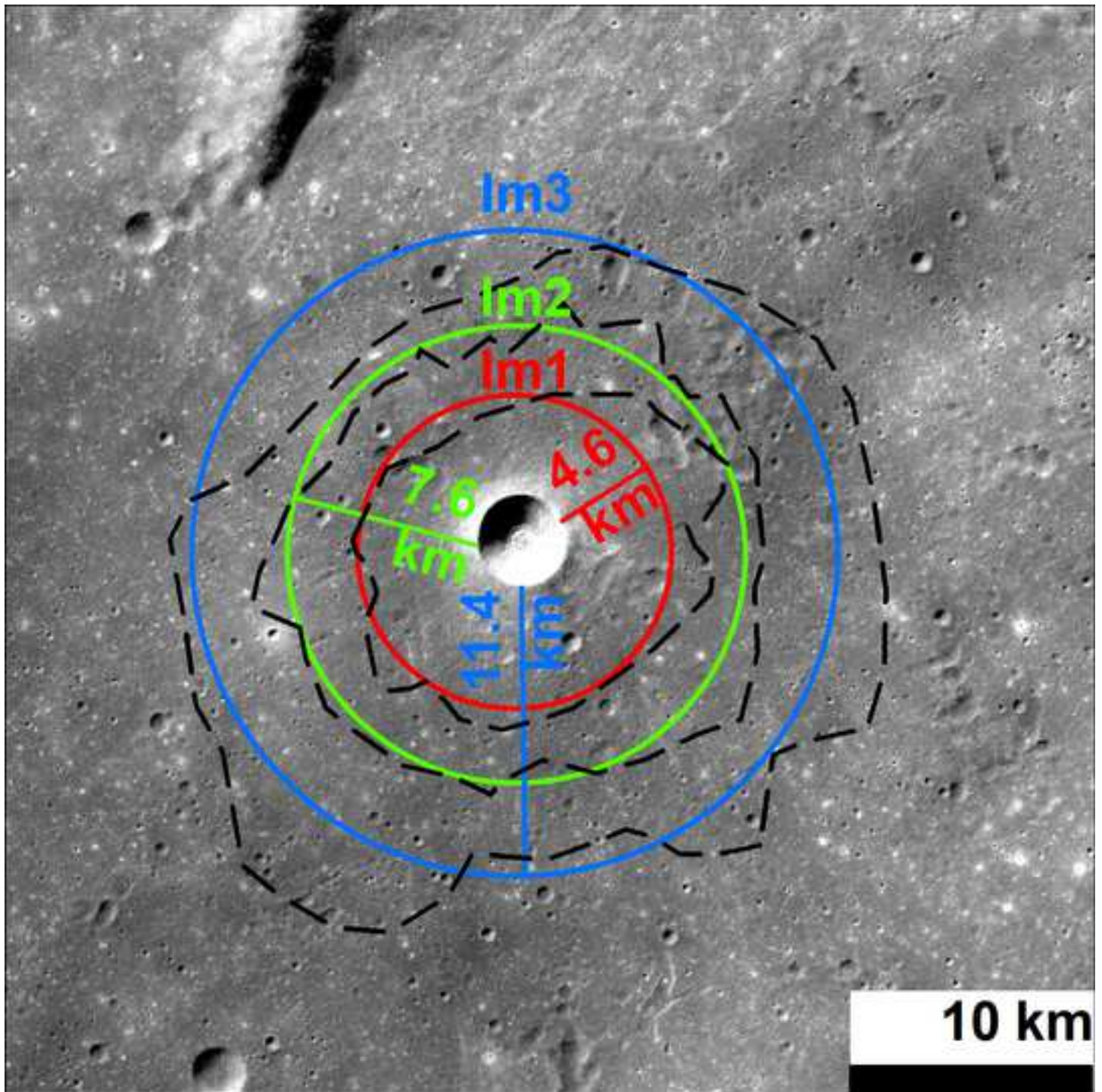
[Click here to access/download;Figure;Fig1_ZhinyuContext_R1.png](#)














Click here to access/download

e-Component

Mare basalt flooding revealed by Zhinyu
crater_SM_1208.docx